Merging of coronal and heliospheric numerical two-dimensional MHD models

D. Odstrcil,[1,5] J. A. Linker,[2] R. Lionello,[2] Z. Mikic,[2] P. Riley,[2] V. J. Pizzo,[3] and J. G. Luhmann[4]

Received 18 February 2002; revised 12 August 2002; accepted 9 September 2002; published 31 December 2002.

[1] Space weather research requires investigation of a complex chain of coupled dynamic phenomena occurring simultaneously on various spatial and temporal scales between the Sun and Earth. Specialized physically based numerical models have been developed to address particular aspects of the entire system. However, an integrated modeling approach is necessary to provide a complete picture suitable for interpretation of various remote and in situ observations and for development of forecasting capabilities. In this paper we demonstrate merging of coronal and heliospheric MHD models for a two-dimensional hypothetical case involving a magnetic cloud, shock, streamer belt, and current sheet. The disruption of a sheared helmet streamer launches a coronal mass ejection (CME) (simulated by the coronal model), which evolves during its propagation through interplanetary space (simulated by the heliospheric model). These models employ different physical approximations and numerical grids to simulate physical phenomena over their respective spatial and temporal domains. The merging of the models enables accurate tracking of a CME from its origin in the solar atmosphere to its arrival at Earth. *INDEX TERMS:* 2111 Interplanetary Physics: Ejecta, driver gases, and magnetic clouds; 7513 Solar Physics, Astrophysics, and Astronomy: Coronal mass ejections; 2139 Interplanetary Physics: Interplanetary shocks; 3230 Mathematical Geophysics: Numerical solutions; *KEYWORDS:* coronal mass injections, magnetic clouds, interplanetary shocks, magnetohydrodynamics, numerical solutions

Citation: Odstrcil, D., J. A. Linker, R. Lionello, Z. Mikic, P. Riley, V. J. Pizzo, and J. G. Luhmann, Merging of coronal and heliospheric numerical two-dimensional MHD models, *J. Geophys. Res.*, *107*(A12), 1493, doi:10.1029/2002JA009334, 2002.

1. Introduction

[2] Space weather research and forecasting involves a complex chain of various dynamic phenomena occurring simultaneously on different spatial and temporal scales. Specialized physically based numerical models have been developed to address particular aspects of the entire system. However, an understanding of the entire chain of dynamic phenomena between the solar atmosphere and Earth's magnetosphere is needed to support space weather applications, in particular to enhance capabilities to forecast geoeffective events of solar origin. Significant progress toward this goal can be achieved by careful merging of the specialized numerical models. This approach will enable the use of existing models to be replaced by more advanced ones in the future and will involve the larger modeling community.

[3] Coronal mass ejections (CMEs) are spectacular manifestations of solar activity. They represent a huge release of solar mass into interplanetary space. CMEs have been identified as the primary link between solar and large nonrecurrent geomagnetic storms [*Gosling*, 1990]; they are believed to be the source of the ''southward'' magnetic fields (relative to the magnetic field at Earth's magnetopause) and interplanetary shock waves that trigger geomagnetic storms. Flux rope-like structures are frequently observed in the solar wind following halo CMEs at the Sun [*Webb et al.*, 2000]. They are generally believed to be the ejecta of CMEs, and *Burlaga et al.* [1982] called them magnetic clouds. *Gosling et al.* [1991] estimated that approximately 30% of interplanetary CMEs have this form. The flux rope magnetic field can initiate geomagnetic activity if it contains fields that are southward relative to the magnetic field at Earth's magnetopause [*Burlaga et al.*, 1987]. A southward magnetic field can also be generated by draping of the ambient solar wind field around the ejecta; a shock wave in front of the ejecta can intensify this field [*Gosling and McComas*, 1987; *Tsurutani et al.*, 1999].

[4] Although significant attention has been given to numerical magnetohydrodynamic (MHD) modeling of CMEs, the focus has generally been divided between considerations of their origin in the solar corona or of their

[1]Cooperative Institute for Research in Environmental Sciences, at University of Colorado, and National Oceanic and Atmospheric Administration, Boulder, Colorado, USA.
[2]Science Applications International Corporation, San Diego, California, USA.
[3]Space Environment Center, National Oceanic and Atmospheric Administration, Boulder, Colorado, USA.
[4]Space Science Laboratory, University of California, Berkeley, California, USA.
[5]On leave from the Astronomical Institute, Ondřejov, Czech Republic.

0148-0227/02/2002JA009334$09.00

propagation in interplanetary space. Very few attempts have been made to simulate these two aspects simultaneously [e.g., *Usmanov and Dryer*, 1995; *Wu et al.*, 1999; *Groth et al.*, 2000]. These simulations were performed using various single, general-purpose numerical codes, and the results illustrate some of the difficulties and limitations of that approach. The very different physics relevant in coronal and interplanetary regimes, the much tighter time step constraints for coronal simulations, and the need to optimize and update individual system components with the latest understanding favor the use of coupled systems of specialized models.

[5] This paper presents the first results from collaborative efforts of the National Science Foundation project "Integrated Space Weather Modeling" conducted by research teams led by Boston University. The coronal and solar wind modeling part is handled by a team of researchers drawn from the University of California in Berkeley, Science Applications International Corporation (SAIC) in San Diego, University of Colorado (CU) in Boulder, and National Oceanic and Atmospheric Administration (NOAA) in Boulder. This paper presents a demonstration of merged coronal and heliospheric two-dimensional (2-D) MHD models.

2. Numerical Models

[6] Simulations of coronal transients (performed at SAIC) provide the input needed to drive heliospheric simulations (performed at CU/CIRES and NOAA/SEC). The coronal model is based on the 2-D axisymmetric resistive MHD equations that are solved by a semi-implicit finite difference scheme using staggered values [*Mikic and Linker*, 1994; *Linker and Mikic*, 1995]. The heliospheric model is based on the 2-D axisymmetric ideal MHD equations that are solved by an explicit finite difference total-variation-diminishing high-resolution Lax-Friedrichs (TVDLF) scheme using cell-centered values [*Odstrcil et al.*, 1996; *Toth and Odstrcil*, 1996; *Odstrcil and Pizzo*, 1999b]. Both numerical models satisfy $\nabla \cdot B = 0$ to roundoff error; this is achieved by computing the vector potential ($A = \nabla \times B$) in the coronal model and by using the field-interpolated central-difference approach for solving the magnetic field [*Toth*, 2000] in the heliospheric model.

[7] The coronal model uses a ratio of specific heats $\gamma = 1.05$ to simulate heat conduction processes and thermal energy sources. The heliospheric model uses $\gamma = 5/3$ to describe fully ionized solar wind plasma, which allows for obtaining accurate shock strengths. We have also performed heliospheric computations with an empirically based $\gamma = 1.5$ which reflects nonideal processes in the solar wind [*Totten et al.*, 1995]. The dynamical differences are small and $\gamma = 5/3$ is used in this paper since the aim is to track the steepening of coronal pressure waves into interplanetary shocks.

[8] Figure 1 shows the merged numerical grids used in the coupled computations. Coronal model computations are performed on a nonuniform mesh with 200 × 300 grid points, with the radial spacing ranging from 0.0053 R_S at the coronal base to 0.59 R_S at the outer boundary. The meridional spacing ranges from 0.24 to 2.4° with the finest resolution in the streamer just below the equatorial plane.

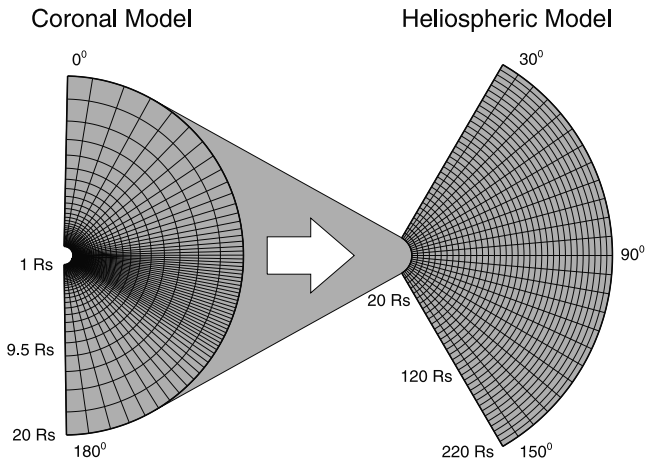

Figure 1. Merged numerical grids. Coronal model computations are performed on a non-uniform mesh, with 200 × 300 grid points, between 1 and 20 R_S shown at the left. Heliospheric model computations are performed on a uniform mesh, with 340 × 240 grid points, between 20 and 220 R_S shown at the right. The output from the coronal model at 20 R_S is used as input for the heliospheric model. Note that only every 5th and 10th grid line is shown in the coronal and heliospheric grids, respectively.

Heliospheric model computations are performed on a uniform mesh with 340 × 240 grid points. The radial and meridional spacings are 0.59 R_S and 0.5°, respectively.

[9] The output from the coronal model consists of a temporal sequence of MHD flow parameters which are used as a boundary condition for the heliospheric solutions. Our scheme stores values on two contiguous spherical surfaces in the upper corona, yielding both values and gradients for a guard-cell approach on the inner boundary of the heliospheric model. In this paper, linear interpolation is used to derive guard-cell values from coronal computations at given time levels (1-hour spacing was found to be adequate) and then to derive guard-cell values at the each numerical time step. We have interpolated values of the vector potential (provided by the coronal model) to derive values of the magnetic field satisfying $\nabla \cdot B = 0$ condition. Details of the interface procedure are given in Appendix A.

3. Ambient State

[10] The coronal simulation starts from an initial potential magnetic field and a spherically symmetric Parker solar wind [*Mikic and Linker*, 1994; *Linker and Mikic*, 1995]. The magnetic flux distribution was chosen to yield a streamer belt that is slightly below and inclined to the solar equatorial plane. The strength of the radial component of the surface magnetic field ranges between −0.441 and 0.335 mT. The plasma number density at the boundary is fixed at 10^8 cm^{-3}, the boundary temperature is 1.8 MK, and the radial velocity is determined at each time step by solving the gas characteristic equations. The Alfven time ($\tau_A = R_S/V_A$) for the above parameters and a mean field strength $B = 0.2205$ mT is 24 min (Alfven speed $V_A = 480$ km/s). A uniform resistivity η is used, corresponding to a Lundquist number $S = 10^5$ (ratio of the resistive time $\tau_r = 4\pi R_S^2/\eta c^2$ to the Alfven time, where c is the speed of light). The viscous

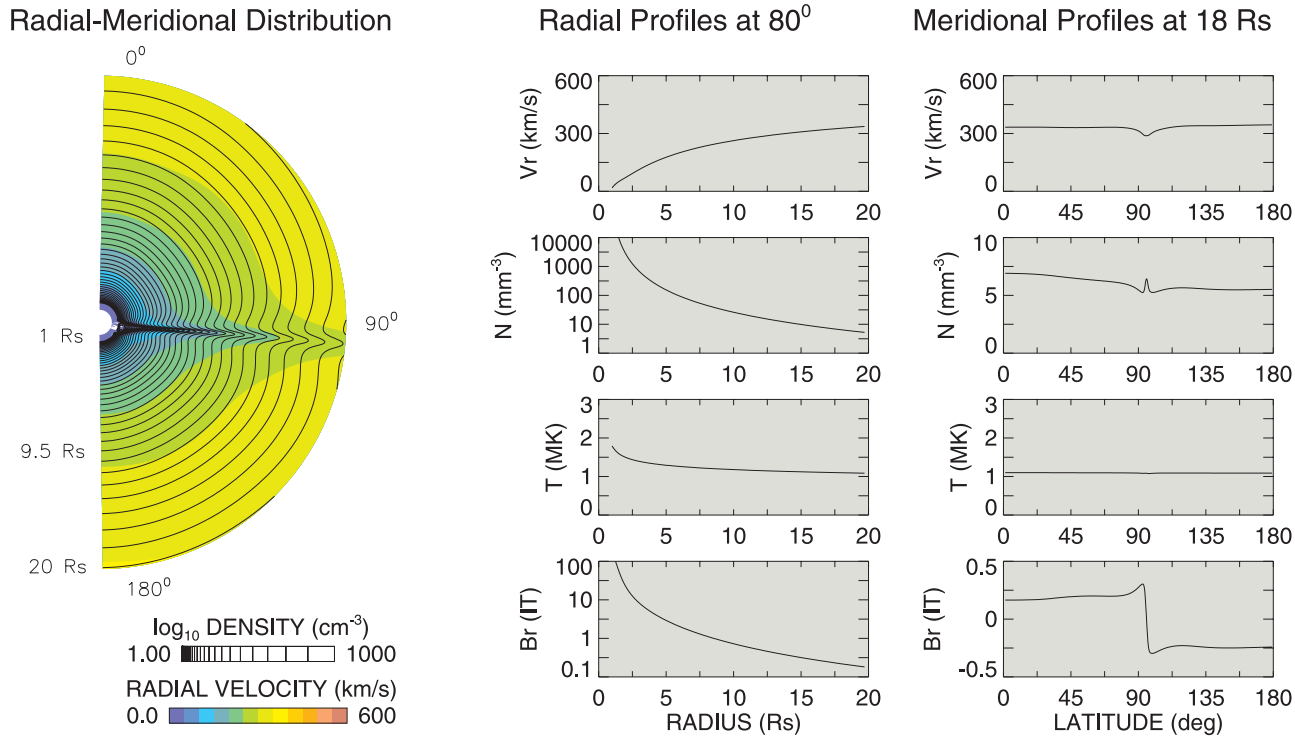

Figure 2. Ambient state of the corona at 250 hours. Distributions of the radial velocity (color scale) and plasma number density (black contours) over the whole computational domain are shown at the left. Profiles of the radial velocity, plasma number density, temperature, and the radial magnetic field at $\theta = 80°$ (radial profiles) and $r = 18$ R_S (meridional profiles) are shown in the center and right, respectively.

diffusion time is $\tau_\nu = R_S^2/\nu = 450\tau_A$, where ν is the viscosity. The 2-D MHD equations are integrated forward in time for 5 days to ensure that a steady state is reached. Figure 2 shows the ambient state in the corona at 250 hours (i.e., at time when a steady state is reached in the heliosphere as well). It corresponds to a streamer configuration characterized by a region of closed magnetic field bounded by a current sheet and open magnetic fields [*Linker and Mikic*, 1995]. Solar rotation is neglected, so the ambient azimuthal field is zero. The streamer belt is slightly below and inclined to the solar equatorial plane in this 2-D simulation.

[11] Heliospheric simulations of the solar wind are driven by flow parameters of the solar corona at 20 R_S. An ambient state is reached by numerical relaxation, i.e., time-dependent computations in the heliospheric domain, starting from the initial state obtained by extrapolating the coronal solution, and using the inner-boundary values given by the coronal solution at 20 R_S.

[12] Figure 3 shows the resulting ambient state in the heliosphere at 250 hours. The heliospheric configuration consists of a dense and slow streamer belt flow near the equatorial plane surrounded by less dense and faster streams in the Northern and Southern Hemispheres. The heliospheric streamer belt has an embedded heliospheric current sheet, and it is ~10% denser and 50 km/s slower than the fast streams. This is a relatively low contrast, which will be improved by incorporation of more realistic heating in the solar corona in future simulations. The ambient, structured solar wind slightly evolves in time, as it reflects changes in the coronal plasma during shearing of the streamer belt.

[13] Figure 4 shows the radial profiles of the plasma parameters in the vicinity of the interface boundary at three different latitudes. The density, radial velocity, and radial magnetic field show smooth transitions between coronal and heliospheric models corresponding to the expanding plasma. The temperature has a sharp change in slope of its radial profile that is caused by the jump in the ratio of specific heats between coronal and heliospheric models ($\gamma = 1.05$ and 5/3, respectively). There is a small kink in the meridional velocity profile at $\theta = 80°$ that identifies readjustment of the streamer belt to different conditions in the heliosphere. The amplitude of this effect is ~1 km/s, which is much less than both the overall expansion speed (~300 km/s at 20 R_S) and the meridional velocities driven by the transient disturbance (~30 km/s; see section 3). At large distances from the streamer belt, the meridional velocity shows a smooth transition (see profile at $\theta = 70°$ in Figure 4).

4. Transient Disturbances

[14] Once the ambient state is established, a shear flow near the neutral line is applied to feed free magnetic energy into the streamer, producing strongly sheared field lines that are nearly aligned with the neutral line, as is frequently observed in filament channels [*Martin et al.*, 1994]. The shearing phase is not intended to model actual flows on the Sun; it is just a convenient mechanism for producing strongly sheared field lines that are nearly aligned with the neutral line [*Amari et al.*, 2000; *Linker et al.*, 2001]. The shearing phase lasts 5.2 days, during which a flow of <2

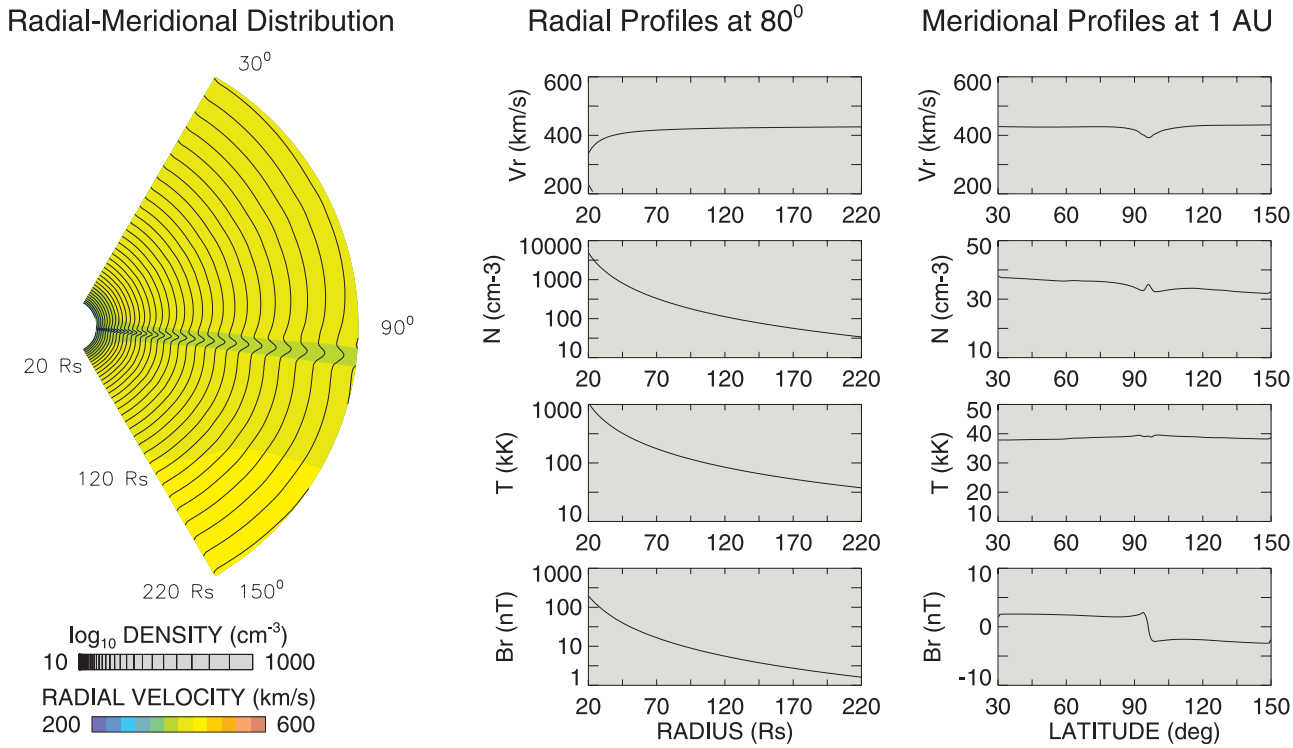

Figure 3. Ambient state of the heliosphere at 250 hours. Distributions of the radial velocity (color scale) and plasma number density (black contours) over the whole computational domain are shown at the left. Profiles of the radial velocity, plasma number density, temperature, and the radial magnetic field at $\theta = 80°$ (radial profiles) and r = 1 AU (meridional profiles) are shown in the center and right, respectively.

km/s is ramped up (4 hours), maintained, and finally ramped down (4 hours). Then we reduce the magnetic flux at the photosphere by ~15% over a period of 20 hours. This leads initially to the formation of a stable magnetic flux rope. The boundary conditions for reducing the flux (flux cancellation) have been described previously [*Amari et al.*, 2000; *Linker et al.*, 2001]. We note that the flows and corresponding electric fields for cancelling flux and emerging flux of opposite polarity at the boundary are the same, i.e., the reconnection at the neutral line that causes detached loops to

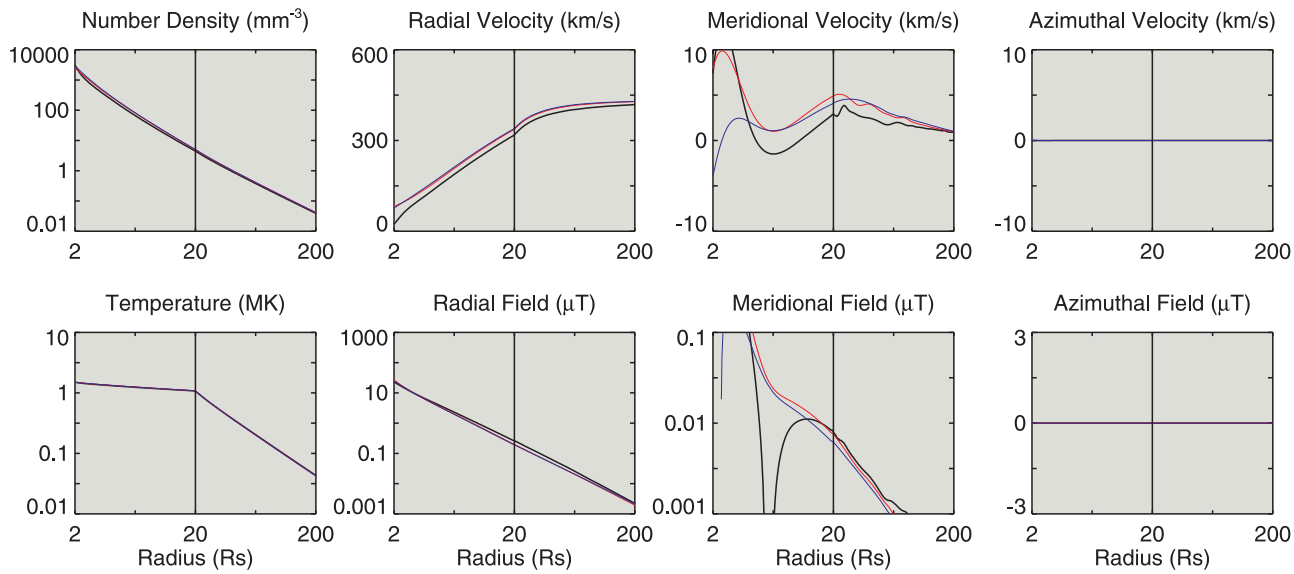

Figure 4. Plasma parameters in the corona and heliosphere as a function of heliospheric distance for the ambient state at 250 hours. Blue, red, and black solid lines correspond to observing positions at 70°, 80°, and 90°, respectively. The interface between coronal and heliospheric models (at 20 R_S) is identified by the vertical black line.

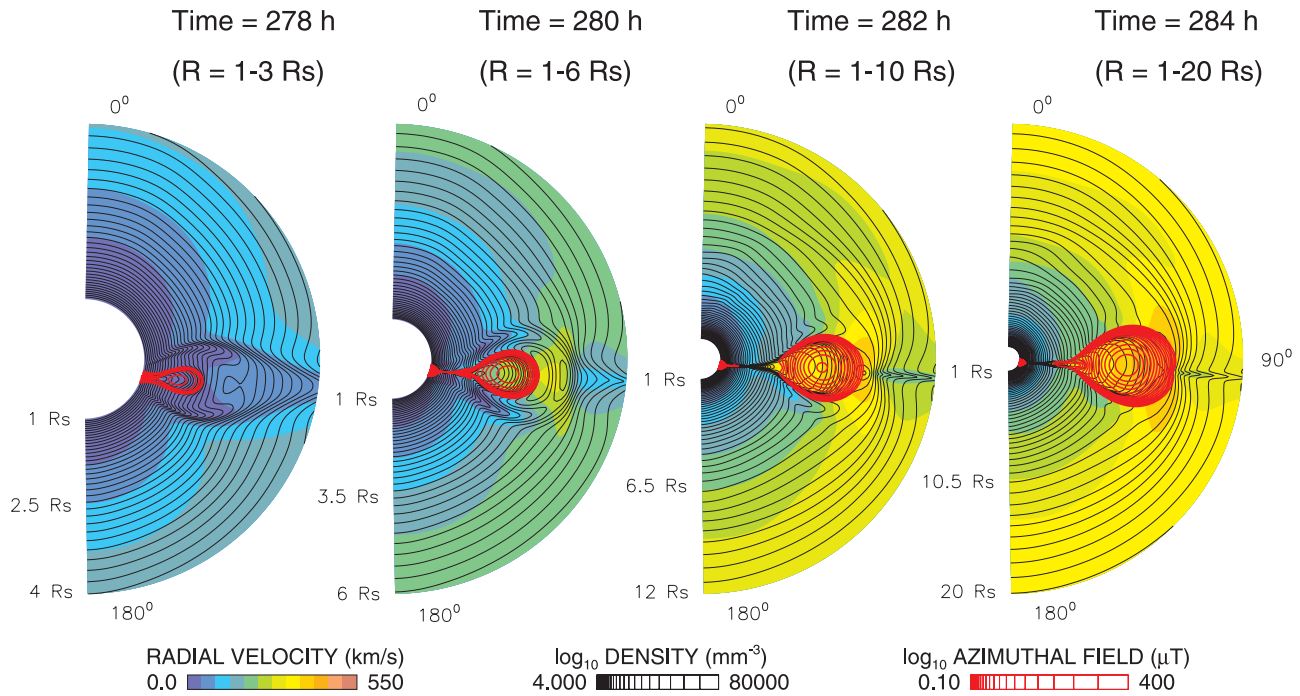

Figure 5. Launch of a CME in the corona. Distributions of the radial velocity (color scale), plasma number density (black contours), and azimuthal magnetic field (red contours) are shown at four different times (278, 280, 282, and 284 hours). Note that the radial extent of the computational domain in each display panel increases progressively with time.

form in the corona also causes submergence of loops. When the flux reduction continues, after ~18 hours (corresponding to 13.5% of flux reduction), the arcade erupts, as shown in Figure 5. The ejected magnetic cloud (flux rope) propagates toward the outer boundary and generates compressive pressure waves ahead of its leading edge.

[15] The temporal evolution of the plasma parameters at 20 R_S (outer boundary of the coronal model) is shown in Figure 6. The magnetic cloud has been identified between 285 and 292 hours as a large increase in the azimuthal field component, and it involves large-scale rotation of the magnetic field in the r-θ plane (seen in the radial and

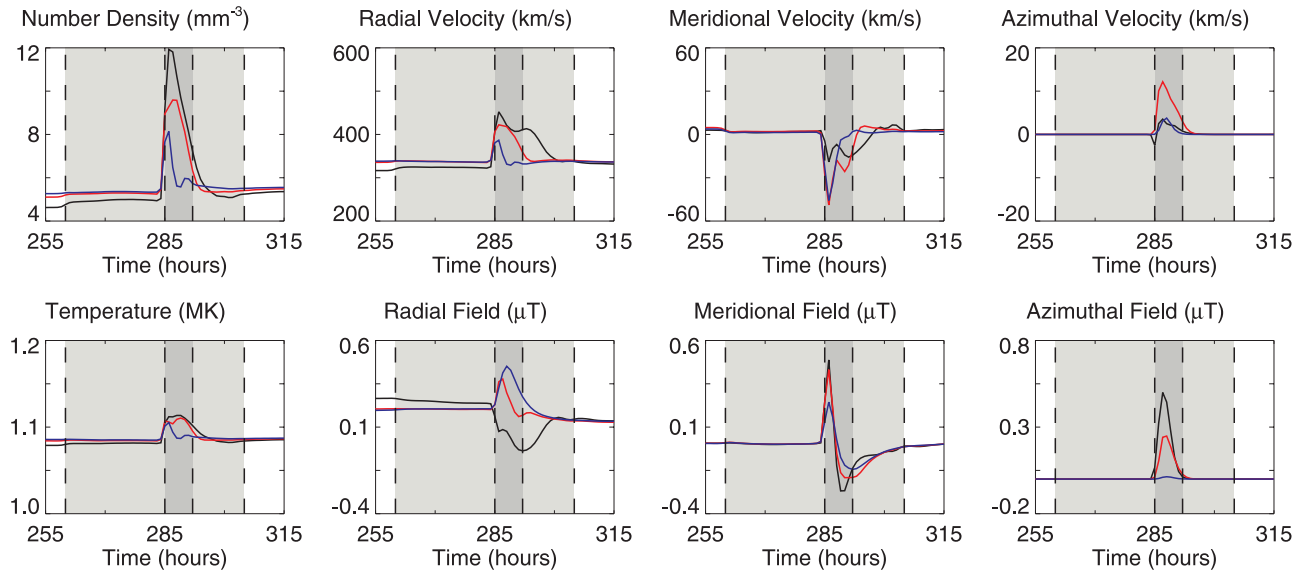

Figure 6. Evolution of coronal plasma parameters as a function of time at 20 R_S. The plasma number density, velocity components, temperature, and magnetic field components are shown at separate panels as indicated. Blue, red, and black solid lines correspond to observing positions at 70°, 80°, and 90°, respectively. Vertical dashed lines mark the pressure wave (260 hours), cloud boundaries (285 and 292 hours), and termination of a rarefaction wave (305 hours) for profiles at 80°.

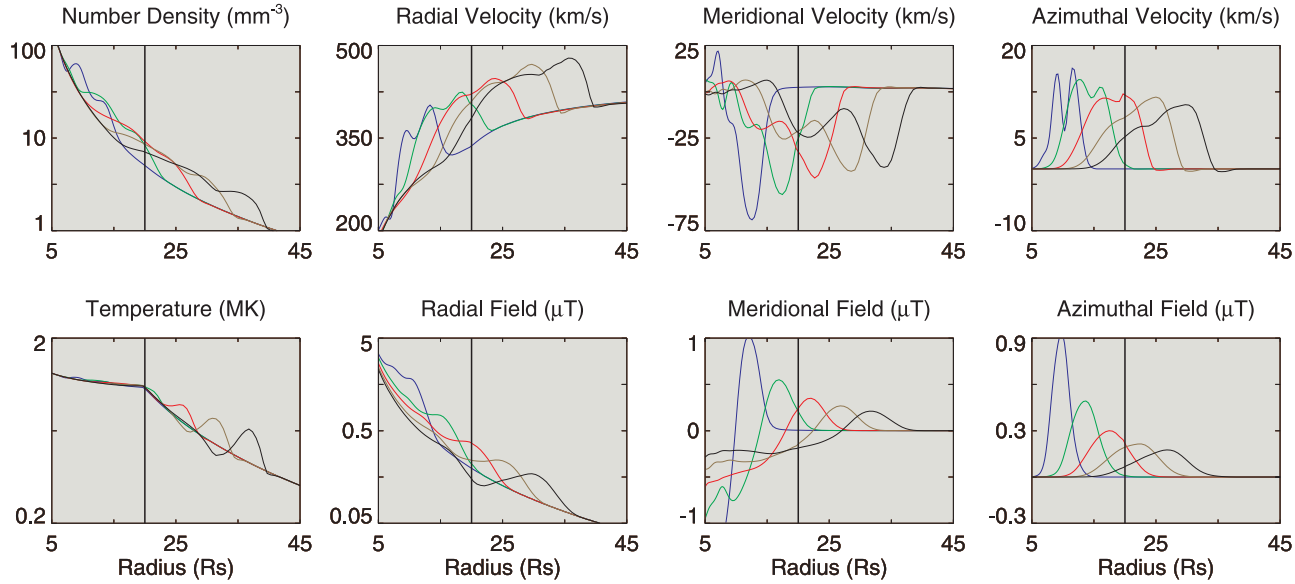

Figure 7. Passage of transient disturbances through the interface boundary at 20 R_S and 80°. The plasma number density, velocity components, temperature, and magnetic field components are shown in separate panels, as indicated. Blue, green, red, brown, and black lines correspond to values at 283, 285, 287, 289, and 291 hours, respectively. Interface between coronal and heliospheric models (at 20 R_S) is identified by the vertical black line.

meridional field components). Note that this field rotation is similar for the magnetic cloud (red line) and external field distorted by the cloud propagation (blue line). The ejected cloud has larger magnetic field, plasma density, and temperature than the external medium and it expands, as can be seen in the velocity profiles (larger value at the leading edge than at the trailing edge). There is a small increase of the density and radial velocity at 260 hours that we identify as a

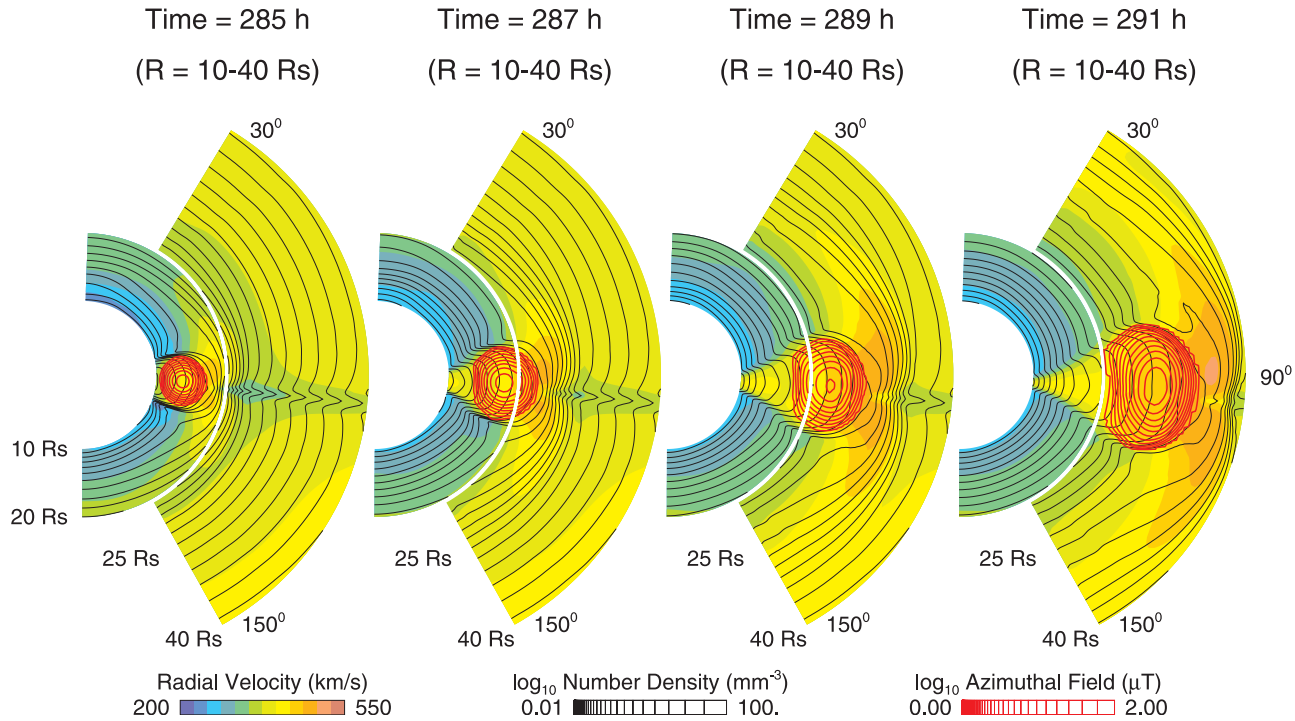

Figure 8. Passage of a CME through the interface boundary between coronal and heliospheric models. Distributions of the radial velocity (color scale), plasma number density (black contours), and azimuthal magnetic field (red contours) are shown at four different times (285, 287, 289, and 291 hours). Note that only the upper and lower portions of the coronal and heliospheric models are depicted. The interface between coronal and heliospheric models (at 20 R_S) is identified by the thick white line.

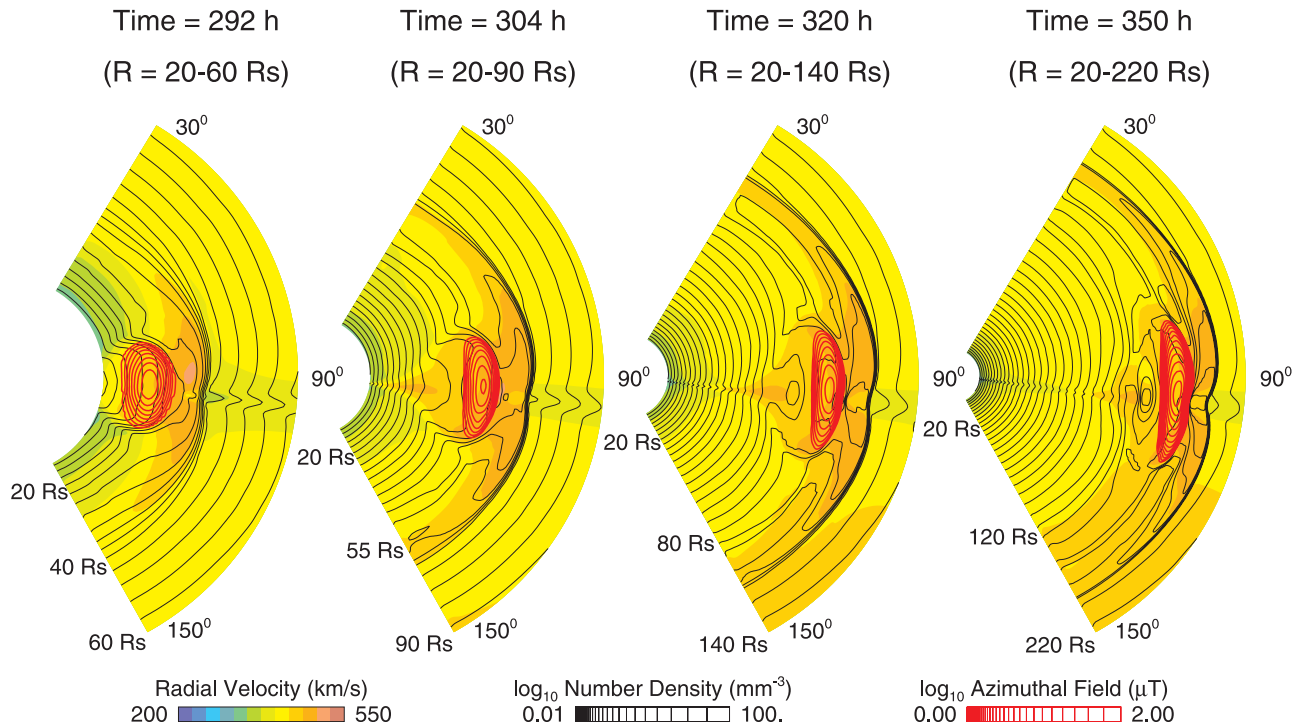

Figure 9. Propagation of a CME in the heliosphere. Distributions of the radial velocity (color scale), plasma number density (black contours), and azimuthal magnetic field (red contours) are shown at four different times (292, 304, 320, and 350 hours). Note the progressively increasing radial extent of the graphical domain.

blast wave associated with the eruptive process in the low corona. The pressure waves driven by the cloud motion are very close to its leading edge (see Figure 5) and they arrive $\sim$1–2 hours earlier.

[16] The passage of the disturbance through the interface between the coronal and heliospheric models is shown in Figures 7 and 8. The transition from one model to the other is smooth, without any obvious artifacts being introduced. Small residual numerical inaccuracies do not appear to affect the global dynamics of both pressure waves and the magnetic flux rope. The distribution of plasma parameters in Figures 7 and 8 shows a significant expansion of the magnetic cloud near the inner heliospheric boundary. The azimuthal components result from the shearing of the coronal streamer belt at the Sun and are uniform throughout the 2-D flux rope formed in the simulation.

[17] The propagation of the magnetic cloud and its associated disturbance in interplanetary space is shown in Figure 9. The initially circular magnetic cloud gradually distorts owing to its interaction with a slower ambient background solar wind. It is squeezed radially and it expands latitudinally. Thus the shape changes from a circular cross section to an elliptical, lentil-like one. Such shape changes have also been observed in other numerical simulations [e.g., *Odstrcil and Pizzo*, 1999a; *Cargill et al.*, 2000].

[18] Coronal compressive pressure waves, driven by the magnetic cloud, propagate into interplanetary space where they steepen into an interplanetary shock (Figure 9). This shock has a distorted front due to its interaction with slower and denser flow in the heliospheric streamer belt ahead [*Odstrcil et al.*, 1996]. The distortion is expected to be greater for larger differences between slow and fast streams [see *Riley et al.*, 1997; *Odstrcil and Pizzo*, 1999a]. Note that steepening of pressure waves is retarded in the solar corona (the nearly isothermal conditions provided by the use of γ =1.05 keeps the characteristic speed of the coronal plasma relatively large and uniform), so that most of it occurs in the heliosphere, where the rapid decline in temperature causes the propagation of the ejected cloud to become super-critical with respect to the local characteristic speed.

[19] The temporal evolution of the heliospheric disturbance at 1 AU is shown in Figure 10. It is quite remarkable that such a range in profiles is found from such a simple input. Clearly, a single CME is capable of producing a wide range of properties depending on the observer's vantage point. The shock ($\approx$357 hours) is followed by the magnetic flux rope ($\approx$368–378 hours) and a trailing rarefaction region ($\approx$378–392 hours). Note that the ambient magnetic field is basically radial, with no azimuthal component, and thus the shock is identified by jumps in the density, temperature, and radial velocity. Further, note that the large-scale magnetic field rotation (see the radial and meridional field components) is similar for the magnetic cloud (red line) and external field distorted by the cloud propagation (blue line). Plasma parameters correspond to typical values observed at the Earth, except for the density which is $\sim$3–4 times too large (this is due to the polytropic approximation in the coronal model; work is currently underway to improve it). The velocity is faster at the leading edge of the cloud than on its trailing edge, suggesting that the CME continues to expand. This is a common feature of magnetic clouds

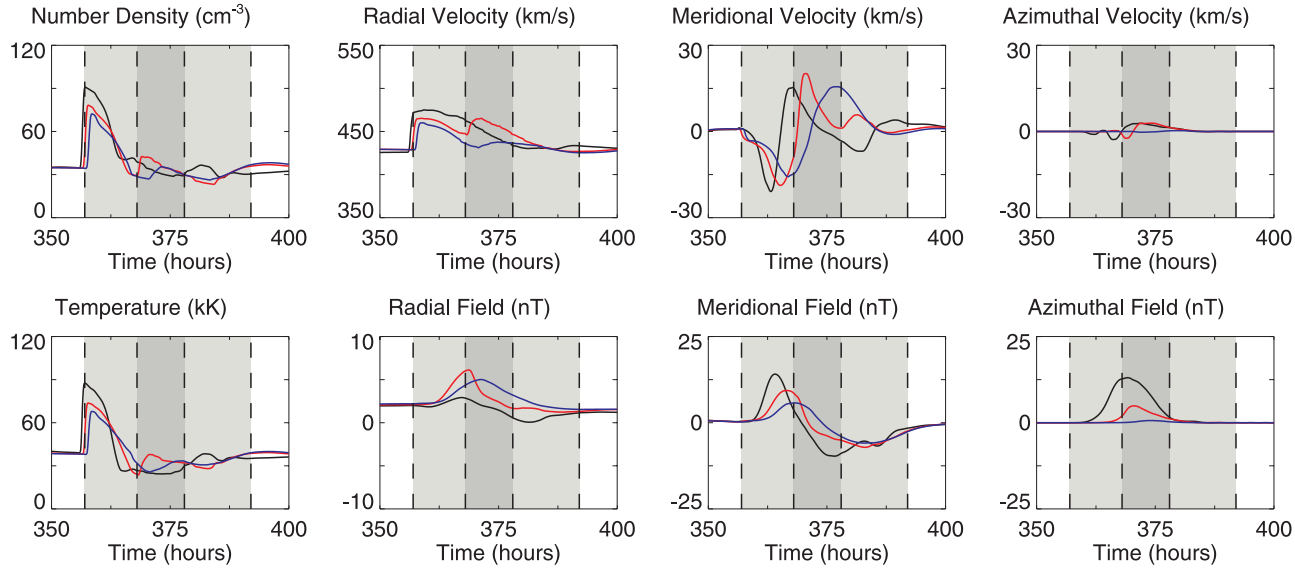

Figure 10. Evolution of interplanetary plasma parameters as a function of time at 1 AU. The plasma number density, velocity components, temperature, and magnetic field components are shown at separate panels as indicated. Blue, red, and black solid lines correspond to observing positions at 70°, 80°, and 90°, respectively. Vertical dashed lines marks the shock (357 hours), cloud boundaries (368 and 378 hours), and termination of the rarefaction wave (392 hours) for profiles at 80°.

observed by the Helios spacecraft between 0.3 and 1 AU [*Bothmer and Schwenn*, 1998].

[20] The magnetic field has a significant meridional component that suggests a possible large geo-effective impact of the simulated event. It includes a draped magnetic field and the ejected flux rope portion. Amplification of the magnetic field by the shock compression is negligible in given observing positions since the shock propagates almost parallel to the magnetic field lines. Note that the sign of the north-south field disturbance would be reversed by a change in the initial large-scale solar magnetic field polarity within this model.

5. Discussion

[21] Numerical simulations of heliospheric disturbances have often been initiated at an inner boundary located in the super-critical flow region. While this simplifies the treatment of boundary conditions and enables the analysis of dynamic phenomena from well-defined situations, such an approach also has its limitations. Merged coronal and heliospheric models allow us to follow the consequences of the solar activity directly and more realistically. Some of the results stemming from this new research tool are discussed below.

[22] In purely heliospheric simulations, interplanetary magnetic clouds are initialized by analytically derived models specified at the inner boundary. Assumptions and approximations involved in this approach largely determine the dynamic evolution of the cloud and results at 1 AU. In coupled coronal and heliospheric simulations the interplanetary magnetic cloud is generated by a magnetic eruption in the solar corona. Such clouds are self-consistent with the surrounding solar wind parameters ab initio. This property is especially important for investigations of more realistic scenarios involving structured solar wind with the heliospheric current sheet.

[23] Compressive pressure waves steepen in the heliosphere, and this leads to the formation of a transient interplanetary shock. In purely heliospheric simulations, such pressure waves are generated by a localized time-dependent pulse or by an injected structure at the inner boundary. In coupled coronal and heliospheric simulations the pressure waves are associated with the launch of the CME. When these coronal waves reach the heliospheric region they have a latitudinal extent larger than the typical extent of pulses or structures used in the heliospheric simulations. Thus the coupled simulation can produce a broad interplanetary shock in contrast to the relatively narrow shocks produced by the heliospheric simulations.

[24] When a fast-moving plasma cloud interacts with a slower ambient background flow the plasma pressure builds up at the leading edge of the cloud, and a shock pair may be formed (with a tangential discontinuity in between that separates the CME plasma from the ambient wind), provided that the injected speed relative to the ambient medium exceeds the medium's characteristic speed. These two shocks propagate in opposite directions to each other; the forward shock is directed away from the Sun and the reverse shock is directed toward it. Where the background flow is super-critical, the reverse shock is convected away from the Sun. This behavior has been observed in early 1-D heliospheric simulations [*Hundhausen and Gentry*, 1969; *Steinolfson et al.*, 1975]. However, reverse shocks have been only rarely observed by space probes [*Gosling et al.*, 1988]. 2-D heliospheric simulations have shown that reverse shocks tend to have smaller angular extent than forward shocks [e.g., *D'Uston et al.*, 1981], and it was suggested that this might explain a discrepancy between numerical modeling and observations. However, the coupled coronal and heliospheric models enable qualitatively different and more realistic simulations. These suggest that a fast-moving plasma cloud interacts strongly with the ambient flow in the

subcritical regions and the reverse pressure waves generated in the process propagate back toward the Sun. Thus reverse shocks are observed in the heliosphere only when the driving plasma clouds form or are still being accelerated at coronal heights beyond the critical point.

[25] The concept of cylindrical magnetic flux ropes has been used to initialize heliospheric simulations in the supercritical region [e.g., *Vandas et al.*, 1996a, 1996b; *Cargill et al.*, 1996, 2000] or to interpret the Helios observations between 0.3 and 1 AU [*Bothmer and Schwenn*, 1998]. This concept seems to be justified in general, since our numerical simulations have demonstrated that a self-consistently launched CME with an embedded magnetic cloud evolves into a cylindrical shape at heliospheric distances near the inner boundary of those models. As the magnetic flux ropes propagate further into heliospheric space, they acquire a lentil-like or concave-outward shape. In these cases, analysis of observations may be better matched using a noncylindrical concept as described by *Mulligan and Russell* [2001].

6. Conclusions

[26] The merging of coronal and heliospheric MHD models has been successfully implemented for a 2-D ambient state and a transient disturbance. The ambient flow is supercritical at the interface between these models, which facilitates coupling the simulations. A transient with a strong magnetic field causes locally subcritical conditions and a problem with over-specified boundary conditions may appear. However, self-consistent coronal results simplify the treatment of heliospheric boundary conditions because they provide self-consistent values needed by the heliospheric model. Thus the specified boundary values seem to be very close to values that would otherwise be obtained by compatible extrapolation from the heliospheric solution. We have it especially important to ensure that $\nabla \cdot B = 0$, in these high-resolution computations, since the low level of intrinsic numerical diffusion is unable to reduce unwanted consequences. Although such consequences might be less important for the global shock structure and flux rope topology they show up in small-scale structures (current sheet, shock interaction, magnetic reconnection). Further, we have found that it is important to evolve the ambient state of the heliospheric calculation by updating values at the inner boundary during both the shearing phase and flux cancellation phase of the coronal calculation prior to the CME initiation. Although the ambient corona and heliosphere evolve slowly during this phase, if one attempts to use constant boundary values (corresponding to the relaxed solar wind solution with a heliospheric current sheet) until just prior to the entrance of the CME into the heliospheric domain, boundary artifacts arise that contaminate the solution. This is also true during the propagation of the CME to 1 AU (even though the ejecta has left the coronal domain entirely).

[27] Different mathematical models, numerical methods, and computational grids were used in this work, and thus the merging of the numerical models was demonstrated for a quite general case. We find this encouraging for the space weather modeling community since it promises to take advantage of the innovative work undertaken by individual specialists and merge it together to provide a more complete picture. For this purpose, a general and flexible framework needs to be developed, and this can be probably realized after acquiring some experience with merging of various existing models.

[28] Merged coronal and heliospheric models have enabled the simulation of transient disturbances that are self-consistent with the background solar wind parameters ab initio. This is difficult or impossible to ensure with analytically derived models of flux ropes initiated in the inner heliosphere (especially for more realistic structured background solar wind). Further, interplanetary shocks form from coronal pressure waves associated with the CME launch, and thus they can have a larger angular extent than shocks generated by localized pulses introduced in the heliosphere. Finally, the formation of reverse shocks or pressure waves (frequently observed in heliospheric simulations) is suppressed since only those formed in the supersonic outflow region will be convected toward the Earth. All these aspects enable more realistic simulations of heliospheric disturbances.

[29] The solar wind and magnetic field parameters at 1 AU resulting from the coupled computations can provide input for geo-effectivity models. We plan to use empirical models to estimate geo-effective indices initially, and work is in progress to provide outputs that can be used by merged magnetospheric-ionospheric-thermospheric models, ultimately leading to a coupled model of the entire solar-terrestrial environment. Work is in progress toward more accurate physical models, interpolation procedures, as well as integrated 3-D MHD models.

Appendix A: Details on Code Merging

[30] In this appendix we describe how our coupling procedure takes into account the different meshes in the two calculations. Further details of the computations will be described in a forthcoming paper devoted to the numerical aspects of the coupled calculations. The coronal (MAS) and heliospheric (ENLIL) codes use different physical models, mathematical descriptions, and numerical methods, which have been described previously [*Mikic and Linker*, 1994; *Linker and Mikic*, 1995; *Linker et al.*, 1999; *Mikic et al.*, 1999; *Lionello et al.*, 1999; *Odstrcil at al.*, 1996; *Toth and Odstrcil*, 1996; *Odstrcil and Pizzo*, 1999b]. Coupled coronal and heliospheric computations require merging of the data structures of these codes in such a way that time-dependent boundary conditions at the inner boundary of the heliospheric model are derived from variables near the outer boundary of the coronal model. The ENLIL code requires knowledge of values at two ghost cells, i.e., two cells just outside the cells in the heliospheric computational domain. These values are derived from output data provided by the MAS code computations as illustrated in Figure A1 and as described below.

[31] Figure A1a shows collocation of variables on the mesh used by the MAS code for coronal computations. The individual cells of the mesh (thin solid lines) have variable size in the r and θ directions. The density (ρ), pressure (P), and azimuthal components of the flow velocity (V_φ) and the vector potential (A_φ) are known at the cell centers (plus symbols); the radial flow velocity (V_r) and meridional magnetic field (B_θ) components are known at the middle

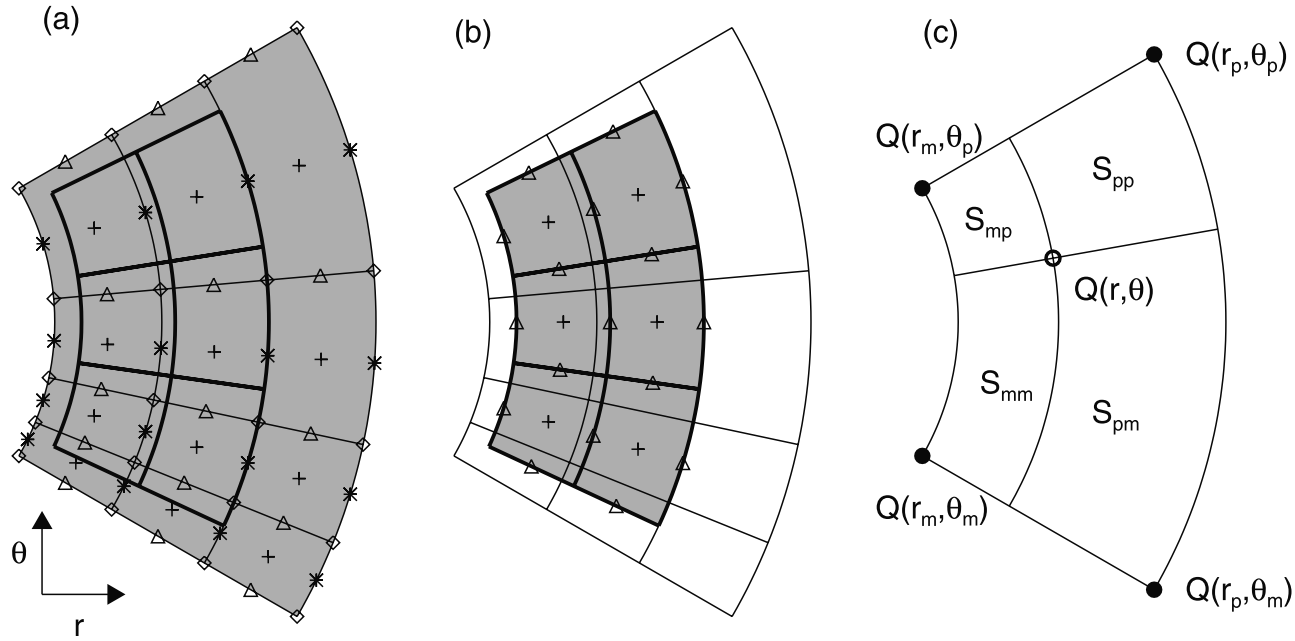

Figure A1. (a) Location of variables on the MAS code mesh. Numerical grid cells are shown by thin solid lines and they are filled by light grey color. Plus symbol marks location of A_φ, V_φ, J_φ, P, and ρ; asterix symbol marks location of V_r and B_θ; triangle symbol marks location of V_θ and B_r; and diamond symbol marks location of B_φ. Thick solid lines mark ghost cells of the ENLIL code. (b) Location of variables on the ENLIL code mesh. Numerical grid cells are shown by thick solid lines and they are filled by light grey color. Plus symbol marks location of ρ, U, V_r, V_θ, V_φ, B_r, B_θ, and B_φ; triangle symbol marks location of A_φ. Thin solid lines mark the MAS code mesh. (c) Quantities used for interpolation of variables from the MAS code mesh (filled circles) into the ENLIL code mesh (open circle). The values of variables at the nearby locations are used for an area-weighted interpolation (relevant areas are labeled as S_{xy}) as described in the text.

of the radial cell interfaces (asterix symbols); and the meridional flow velocity (V_θ) and radial magnetic field (B_r) components are known at the middle of the meridional cell interfaces (triangle symbols). Note that the radial and meridional components of the flow velocity and magnetic field are collocated differently. The thick solid line shows the ''ghost'' cells (i.e., cells just outside the computational domain) of the ENLIL code; the outermost radial boundary is identical with the radial boundary of the MAS-code cells near the end of the coronal domain.

[32] Figure A1b shows collocation of variables on the mesh used by the ghost cells of the ENLIL code for heliospheric computations. The density (ρ), total or thermal energy (U), and components of the flow velocity (V_r, V_θ, V_φ) and magnetic field (B_r, B_θ, B_φ) are to be determined at the cell centers (plus symbols) and the azimuthal component of the vector potential (used as an auxiliary variable at the inner boundary) is to be determined at the cell interfaces (triangle symbols).

[33] Figure A1c illustrates quantities used in the interpolation procedure between the two computational meshes. The value of the quantity Q located at (r, θ) is determined from the nearby quantities using a linear, area-weighted interpolation

$$SQ(r,\theta) = S_{pp}Q(r_m,\theta_m) + S_{pm}Q(r_m,\theta_p) + S_{mp}Q(r_p,\ \theta_m) + S_{mm}Q(r_p,\ \theta_p),$$

where S_{pp}, S_{pm}, S_{mp}, and S_{mm} are respective areas as given in Figure A1c and S is their sum. For example, $S_{mm} = (r - r_m)1/2(r + r_m)(\theta - \theta_m)$. This interpolation procedure enables determination of values at the ghost cells at the inner boundary of the heliospheric model from known values on the coronal mesh provided by the coronal model.

[34] The above interpolation procedure is used to obtain values of the density (ρ), pressure (P), all components of the flow velocity (V_r, V_θ, V_φ), the azimuthal component of the magnetic field (B_φ), and the azimuthal component of the vector potential (A). Note that all values are obtained at the cell centers except the values of the vector potential that are obtained at centers of the cell interfaces (see Figure A1). Then values of the radial and meridional components of the magnetic field components are derived at cell centers from the vector potential ($B = \nabla \times A_\varphi$). Finally, the total energy and the momentum components are computed at the cell centers. Thus all variables needed for the heliospheric computations are specified at the centers of the ghost cells and they are used as time-dependent boundary conditions.

[35] We have tested the coupling procedure described here by examining the propagation of a flux rope configuration in a single domain extending from 20 to 220 R_S and in a split domain (20–120 R_S and 120–220 R_S) with different mesh resolutions. The resulting evolution was essentially the same for both cases. We will describe this and other tests of the coupling procedure in a forthcoming paper.

[36] **Acknowledgments.** We are grateful to the referees for their comments and suggestions. This work was supported by NSF ATM000950 grant. Additional support was from NASA Sun-Earth Connection Theory and Supporting Research and Technology Programs and by grant A3003003 from the Academy of Sciences of the Czech Republic. Computational facilities were provided by National Center for Atmospheric Research in Boulder, Colorado and San Diego Supercomputer Center in San Diego, California.

[37] Shadia Rifai Habbal thanks Peter Cargill and another referee for their assistance in evaluating this paper.

References

Amari, T., J. F. Luciani, Z. Mikic, and J. A. Linker, A twisted flux rope model for coronal mass ejections and two-ribbon flares, *Astrophys. J.*, *529*, L49–L52, 2000.

Bothmer, V., and R. Schwenn, The interplanetary and solar causes of major geomagnetic storms, *J. Geomagn. Geoelectr.*, *47*, 1127–1132, 1995.

Bothmer, V., and R. Schwenn, The structure and origin of magnetic clouds in the solar wind, *Ann. Geophys.*, *16*, 1–24, 1998.

Burlaga, L. F., L. Klein, N. R. Sheeley Jr., D. J. Michels, R. A. Howard, M. J. Koomen, R. Schwenn, and H. Rosenbauer, A magnetic cloud and a coronal mass ejection, *Geophys. Res. Lett.*, *9*, 1317–1320, 1982.

Burlaga, L. F., K. W. Behannon, and L. W. Klein, Compound streams, magnetic clouds, major geomagnetic storms, *J. Geophys. Res.*, *92*, 5725–5734, 1987.

Cargill, P. J., J. Chen, D. S. Spicer, and S. T. Zalesak, MHD simulations of the motion of magnetic flux tubes through a magnetized plasma, *J. Geophys. Res.*, *101*, 4855–4870, 1996.

Cargill, P. J., J. Schmidt, D. S. Spicer, and S. T. Zalesak, Magnetic structure of over-expanding coronal mass ejections: Numerical Models, *J. Geophys. Res.*, *105*, 7509–7519, 2000.

D'Uston, C. M., M. Dryer, S. M. Han, and S. T. Wu, Spatial structure of flare associated perturbations in the solar wind simulated by a two-dimensional numerical MHD code, *J. Geophys. Res.*, *86*, 525–534, 1981.

Gosling, J. T., and D. J. McComas, Field line draping about fast coronal mass ejecta: A source of strong out-of-the-ecliptic interplanetary magnetic fields, *Geophys. Res. Lett.*, *14*, 355–358, 1987.

Gosling, J. T., S. J. Bame, E. J. Smith, and M. E. Burton, Forward-reverse shock pairs associated with transient disturbances in the solar wind at 1 AU, *J. Geophys. Res.*, *93*, 8741–8746, 1988.

Gosling, J. T., Coronal mass ejections and magnetic flux ropes in interplanetary space, in Physics of Magnetic Flux Ropes, *Geophys. Monogr. Ser.*, vol. 58, edited by C. J. Russell, E. R. Priest, L. C. Lee, pp. 343–364, AGU, Washington, D. C., 1990.

Gosling, J. T., D. J. McComas, T. L. Phillips, and S. J. Bame, Geomagnetic activity associated with Earth passage of interplanetary shock disturbances and coronal mass ejections, *J. Geophys. Res.*, *96*, 7831–7839, 1991.

Groth, C. P. T., D. L. DeZeeuw, T. I. Gombosi, and K. G. Powell, Global three-dimensional MHD simulation of a space weather event: CME formation, interplanetary propagation, interaction with the magnetosphere, *J. Geophys. Res.*, *105*, 25,053–25,078, 2000.

Hundhausen, A. J., and R. A. Gentry, Numerical simulation of flare-generated disturbances in the solar wind, *J. Geophys. Res.*, *74*, 2908–2918, 1969.

Linker, J. A., and Z. Mikic, Disruption of a helmet streamer by photospheric shear, *Astrophys. J.*, *438*, L45–L48, 1995.

Linker, J. A., Z. Mikic, D. A. Biesecker, R. J. Forsyth, S. E. Gibson, A. J. Lazarus, A. Lecinski, P. Riley, A. Szabo, and B. J. Thompson, Magnetohydrodynamic modeling of the solar corona during Whole Sun Month, *J. Geophys. Res.*, *104*, 9809–9830, 1999.

Linker, J. A., R. Lionello, Z. Mikic, and T. Amari, Magnetohydrodynamic modeling of prominence formation within a helmet streamer, *J. Geophys. Res.*, *106*, 25,165–25,176, 2001.

Lionello, R., Z. Mikic, and J. A. Linker, Stability of algorithms for waves with large flows, *J. Comput. Phys.*, *152*, 346, 1999.

Martin, S. F., R. Bilimoria, and P. W. Tracadasi, Magnetic field configurations basic to filament channels and filaments, in *Solar Surface Magnetism*, edited by R. J. Rutten and C. J. Schrijver, pp. 303–338, Kluwer Acad., Norwell, Mass., 1994.

Mikic, Z., and J. A. Linker, Disruption of coronal magnetic arcades, *Astrophys. J.*, *430*, 898–912, 1994.

Mikic, Z., J. A. Linker, D. D. Schnack, R. Lionello, and A. Tarditi, Magnetohydrodynamic modeling of the global corona, *Phys. Plasmas*, *6*, 2217–2224, 1999.

Mulligan, T., and C. T. Russell, Multispacecraft modeling of the flux rope structure of interplanetary coronal mass ejections: Cylindrically symmetric versus nonsymmetric topologies, *J. Geophys. Res.*, *106*, 10,581–10,596, 2001.

Odstrcil, D., and V. J. Pizzo, Three-dimensional propagation of coronal mass ejections (CMEs) in a structured solar wind flow, 1, CME launched within the streamer belt, *J. Geophys. Res.*, *104*, 483–492, 1999a.

Odstrcil, D., and V. J. Pizzo, Distortion of interplanetary magnetic field by three-dimensional propagation of CMEs in a structured solar wind, *J. Geophys. Res.*, *104*, 28,225–28,239, 1999b.

Odstrcil, D., M. Dryer, and Z. Smith, Propagation of an interplanetary shock along the heliospheric plasma sheet, *J. Geophys. Res.*, *101*, 19,973–19,984, 1996.

Riley, P., J. T. Gosling, and V. J. Pizzo, A two-dimensional simulation of the radial and latitudinal evolution of a solar wind disturbance driven by a fast, high-pressure coronal mass ejection, *J. Geophys. Res.*, *102*, 14,677–14,685, 1997.

Steinolfson, R. S., M. Dryer, and Y. Nakagawa, Numerical MHD simulation of interplanetary shock pairs, *J. Geophys. Res.*, *80*, 1223–1231, 1975.

Toth, G., The $\nabla \cdot B = 0$ constraint in shock-capturing magnetohydrodynamic codes, *J. Comput. Phys.*, *161*, 605–652, 2000.

Toth, G., and D. Odstrcil, Comparison of some flux corrected transport and total variation diminishing numerical schemes for hydrodynamic and magnetohydrodynamic problems, *J. Comput. Phys.*, *128*, 82–100, 1996.

Totten, T. L., J. W. Freeman, and S. Arya, An empirical determination of the polytropic index for the free-streaming solar wind using HELIOS 1 data, *J. Geophys. Res.*, *100*, 13–17, 1995.

Tsurutani, B. T., Y. Kamide, J. K. Arballo, W. D. Gonzales, and R. P. Lepping, Interplanetary causes of great and superintense magnetic storms, *Phys. Chem. Earth, Ser. C*, *24*, 101–105, 1999.

Usmanov, A. V., and M. Dryer, A global 3-D simulation of interplanetary dynamics in June 1991, *Solar Phys.*, *159*, 347–370, 1995.

Vandas, M., S. Fischer, M. Dryer, Z. Smith, and T. Detman, Simulation of magnetic cloud propagation in the inner heliosphere in two dimensions, 2, A loop parallel to the ecliptic plane and the role of helicity, *J. Geophys. Res.*, *101*, 2505–2510, 1996a.

Vandas, M., S. Fischer, M. Dryer, Z. Smith, and T. Detman, Parametric study of loop-like magnetic cloud propagation, *J. Geophys. Res.*, *101*, 15,645–15,652, 1996b.

Webb, D. F., E. W. Cliver, N. U. Crooker, O. C. St. Cyr, and B. J. Thompson, Relationship of halo coronal mass ejections, magnetic clouds, magnetic storms, *J. Geophys. Res.*, *105*, 7491–7508, 2000.

Wu, S. T., W. P. Guo, D. J. Michels, and L. F. Burlaga, MHD description of the dynamical relationships between a flux rope, streamer, coronal mass ejection, magnetic cloud: An analysis of the January 1997 Sun-Earth connection event, *J. Geophys. Res.*, *104*, 14,789–14,802, 1999.

J. A. Linker, R. Lionello, Z. Mikic, and P. Riley, Science Applications International Corporation, 10260 Campus Point Drive, San Diego, CA 92121, USA. (Jon.A.Linker@saic.com; Roberto.Lionello@saic.com; Zoran.Mikic@saic.com; Peter.Riley@saic.com)

J. G. Luhmann, Space Science Laboratory, University of California, Berkeley, CA 94720, USA. (jgluhman@ssl.berkeley.edu)

D. Odstrcil and V. J. Pizzo, NOAA, Space Environment Center, 325 Broadway, Boulder, CO 80305, USA. (Dusan.Odstrcil@noaa.gov; Victor.J.Pizzo@noaa.gov)